Applied Physics Letters ARTICLE scitation.org/journal/apl

Direct current microplasma formation around microstructure arrays

Cite as: Appl. Phys. Lett. **118**, 174101 (2021); doi: 10.1063/5.0046312
Submitted: 2 February 2021 · Accepted: 14 April 2021 ·
Published Online: 27 April 2021

Yangyang Fu,[1,a)] Huihui Wang,[2] Bocong Zheng,[3,a)] Peng Zhang,[4] Qi Hua Fan,[3,4,5] Xinxin Wang,[1] and John P. Verboncoeur[4,6]

AFFILIATIONS

[1]Department of Electrical Engineering, Tsinghua University, Beijing 100084, China
[2]EMD Performance Materials, Tempe, Arizona 85224, USA
[3]Fraunhofer Center for Coatings and Diamond Technologies, Michigan State University, East Lansing, Michigan 48824, USA
[4]Department of Electrical and Computer Engineering, Michigan State University, East Lansing, Michigan 48824, USA
[5]Department of Chemical Engineering and Materials Science, Michigan State University, East Lansing, Michigan 48824, USA
[6]Department of Computational Mathematics, Science and Engineering, Michigan State University, East Lansing, Michigan 48824, USA

[a)]**Authors to whom correspondence should be addressed:** fuyangyang@tsinghua.edu.cn and bzheng@fraunhofer.org

ABSTRACT

We demonstrate the formation and transition behaviors of a microplasma around microstructure arrays at different gas pressures via two-dimensional particle-in-cell/Monte Carlo collision simulations. It is found that the microdischarge occurs outside the cathode microcavities at the lowest pressure and starts penetrating the microcavities with a curved sheath edge as the pressure increases. At higher pressure, coupled periodic microhollow cathode discharges (MHCDs) are formed inside the microcavities. Further increasing the gas pressure results in the disappearance of the MHCDs, and the dominant discharge shifts outside of the microcavity, locating above the protrusion tips. The effect of the space charge shielding on the discharge and the conditions for MHCD formation are discussed. The macroscopic discharge parameter scalings with the gas pressure and the electron kinetics are also examined. The results are helpful for deeply understanding the microplasma formation with nonplanar electrodes, which inform the scaling, design, and optimization of microplasma array devices across a wide range of pressure regimes in practical applications.

Microplasmas have received growing attention during the past decades due to their potential for a wide range of applications, such as photonic crystals,[1] excimer sources,[2] analytical chemistry,[3] thin film synthesis,[4] and plasma medicine.[5] Various discharge configurations have been utilized for the generation of microplasmas, including dielectric barrier discharges,[6] microplasma jets,[7] microhollow cathode discharges (MHCDs),[8] and others.[9–13] Microplasma devices with independently addressable microcavities for light sources and control electronics have been comprehensively studied by Eden's group.[14–16] Hopwood *et al.* studied the ignition of microwave microplasma with microstrip resonators and presented the scale-up microplasma using an array concept.[17,18] Kushner's group investigated the microplasma array for controlling the propagation of electromagnetic waves and found that the transmitted power can be tuned by the spatial distribution of microplasma cells.[19] More recently, a microdischarge array device with dielectric holes was fabricated as an ozone generator with flexible performance and high efficiency achieved.[20] With recent advances in microfabrication technologies, the configurations of microplasma devices are becoming increasingly diverse.

Although many applications of microplasma devices have been developed, diagnosing the microdischarges is still rather challenging due to the significantly reduced gap dimensions. The conventional probe measurement (e.g., Langmuir probe[21]) and the spectroscopy technique are hardly possible for precise spatially resolved diagnosis. Numerical simulations based on hydrodynamic and fully kinetic models are powerful tools and widely utilized to understand the fundamental mechanisms of the microplasmas.[22–27] However, many of the simulation studies were carried out for planar electrodes or focusing on a single unit between nonplanar electrodes for simplicity. The simulation with ideal planar electrodes cannot characterize the effect of the surface morphology on the discharge. For the simulation with a single unit between nonplanar electrodes, if the periodic boundary

condition is used, the plasma is assumed to be duplicate periodically in the radial direction, and the sidewall effect is just ignored; on the other hand, if the boundary in a single unit is treated as a sidewall, the microplasma will be largely affected by the sidewall since the sheath region can occupy a considerable part of the microgap. Therefore, simplified simulation setups may not fully reflect the practical conditions, which typically have many structural units and a sealed sidewall. Our previous studies have characterized the effect of the nonplanar electrode surface morphology (e.g., hemispherical cathode protrusion) on microgap breakdown.[28–30] Nevertheless, the investigation of microdischarge around nonplanar perturbations is far from complete, and the physics of how a microplasma responds to a multidimensional surface morphology is still not fully understood.

In this work, we demonstrate the generation and characteristics of a microplasma around the microstructure arrays on the cathode surface in a microgap. The transition behaviors of the microdischarge at different pressures are characterized using two-dimensional particle-in-cell/Monte Carlo collision (PIC/MCC, 2d3v) simulations. It is found that the discharges are above the microcavity at lower pressure and localized to the microstructures at higher pressure. The macroscopic discharge parameter scalings with the gas pressure and the electron kinetics is presented. The results from this work provide more comprehensive understanding and better optimization of the operation of microplasma array devices with structured electrodes in practical applications.

The schematic slice of the microgap in Cartesian geometry (xy) is shown in Fig. 1. The microgap consists of one planar anode and a structured cathode with an array of microcavities. A direct-current voltage V_{dc} is applied to the anode through a ballast resistor R_b, while the cathode is grounded. d_1 and d_2 are the shortest and longest gap distance, respectively; w_1 and w_2 are the protrusion width and cavity width, respectively; w_3 is the distance between the outer cavity and the cathode edge. In this work, the discharge conditions are $V_{dc} = 800$ V, $R_b = 100\,\text{k}\Omega$, $d_1 = 150\,\mu$m, $d_2 = 200\,\mu$m, $w_1 = 50\,\mu$m, $w_2 = 50\,\mu$m, and $w_3 = 100\,\mu$m. The microgap in the z-direction is ideally uniform, and since the external circuit is considered, the depth is set to 100 μm,

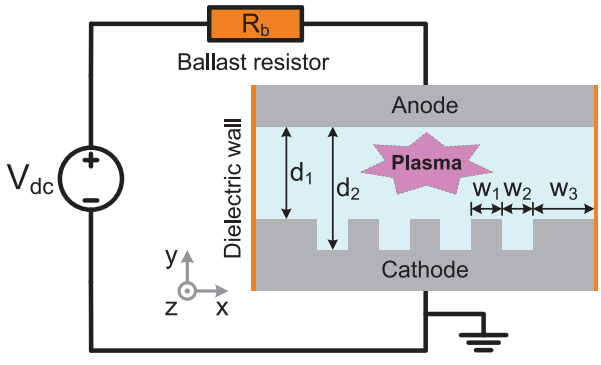

FIG. 1. Schematic of the microgap with the structured cathode and dielectric sidewall in Cartesian geometry (xy). V_{dc} is the applied voltage and R_b is the ballast resistor; d_1 and d_2 are the shortest and longest gap distance, respectively; w_1 and w_2 are the protrusion width and cavity width, respectively; w_3 is the distance between the outer cavity and the cathode edge. In this work, $V_{dc} = 800$ V, $R_b = 100\,\text{k}\Omega$, $d_1 = 150\,\mu$m, $d_2 = 200\,\mu$m, $w_1 = 50\,\mu$m, $w_2 = 50\,\mu$m, and $w_3 = 100\,\mu$m.

in order to determine the discharge conditions in the modeling. The ion-impact secondary electron emission from the cathode is considered, and the effective secondary electron emission coefficient is 0.1.[22] A Neumann boundary condition is used at the inner dielectric sidewall with surface charge accumulation, and $\partial\phi/\partial x = 0$ for the electric potential is used at $x = 0$ and 550 μm. The simulations are performed with argon at 300 K, accounting for three electron–neutral collisions (elastic, excitation, and ionization scattering) and two ion-neutral collisions (isotropic and backward scattering).[31]

The simulations are conducted using a custom-developed two-dimensional PIC/MCC model (Astra code[32]) with an implicit algorithm. The gas pressure p varies from 10 Torr to 200 Torr. For the cases with $p > 50$ Torr, the cell sizes are $\Delta x = \Delta y = 1\,\mu$m, and the time step is $\Delta t = 0.1$ ps. Since implicit algorithm and energy conservation scheme used here alleviate the constraints of the space and time steps, $\Delta x = \Delta y = 2\,\mu$m and $\Delta t = 0.2$ ps are used to accelerate the simulation at lower pressure, which generally takes a longer physical time to reach a steady state. The results presented in the following are from the simulations at the steady state. The number of superparticles in our simulations is on the order of one million and case dependent. The maximum number of superparticles per cell (not the averaged number) is around 100 at lower pressures and about 150∼300 at higher pressures (with smaller discharge regions). Although the collision frequency approaches the plasma frequency for higher pressure cases (e.g., with a larger pd value), under which conditions strictly converged simulations may not be easily obtained with reasonable computational cost, the phenomena occurring predominantly in the sheath region, such as the discharge impedance and the power deposition, can still be adequately captured.[33,34] The same discharge characteristics were also observed in the simulations even using fewer superparticles. Our simulations combined with the implicit algorithm and energy conservation scheme can substantially alleviate the self-heating,[32,35] which ensures the fidelity of the simulation results.

The spatial distributions of the electron density are shown in Fig. 2, demonstrating the transition behaviors of the microdischarge at different pressures. The gas pressure in Figs. 2(a)–2(f) is 10, 20, 50, 100, 150, and 200 Torr, respectively. In Fig. 2(a), the electron density is concentrated above the structured cathode and relatively uniform in the center. The discharge is less perturbed by the irregularity of the cathode. Since the sheath width d_s is larger than the microcavity dimension ($d_s > w_2 = 50\,\mu$m at 10 Torr), the perturbation of the nonplanar structures is screened because of the space charge shielding effect. The density profile is smoothed away from the cathode, and the sheath edge is relatively flat. In Fig. 2(b), the plasma sheath becomes narrower at a higher pressure, and the perturbation of the electrode irregularity is observed. There are multiple electron density peaks right above the cathode microcavities with the maximum electron density increased. The cathode sheath edge is curved, which demonstrates the impact of the nonplanar electrode. In Fig. 2(c), the sheath edge becomes more curved, and the maximum electron density is further increased; the electron density peaks start penetrating the microcavities. At 100 Torr, the MHCDs are formed [see Fig. 2(d)], and the electron density is significantly enhanced, reaching on the order of 10^{21} m^{-3}. Meanwhile, the negative glow region outside the cavity becomes less pronounced. In Fig. 2(e), at 150 Torr, the maximum electron density slightly decreases, while the discharge is still in the MHCD mode. However, further increasing the gas pressure results in the disappearance of the

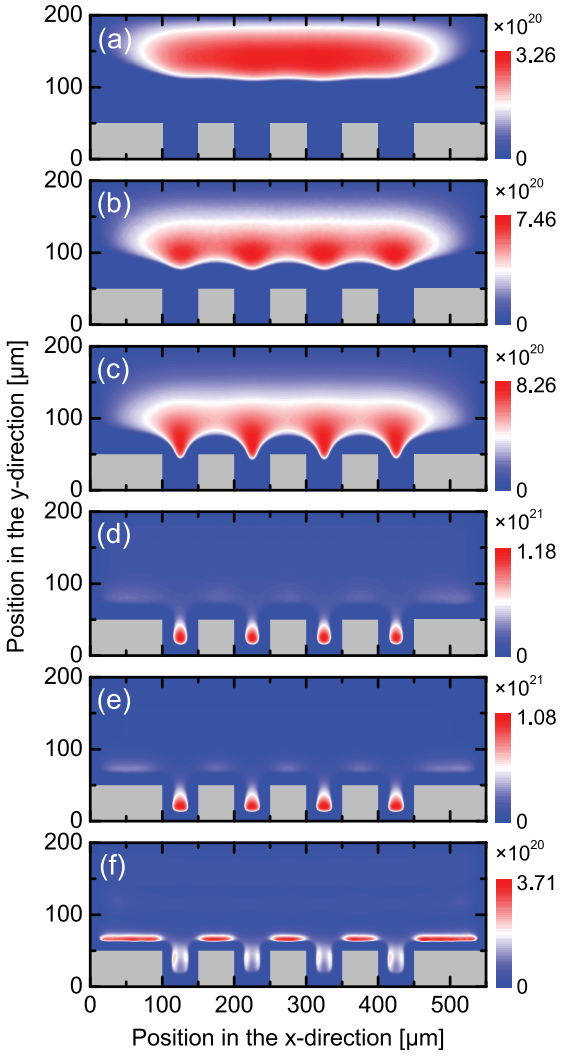

FIG. 2. Spatial distributions of the electron density n_e (unit in m^{-3}) at (a) 10 Torr, (b) 20 Torr, (c) 50 Torr, (d) 100 Torr, (e) 150 Torr, and (f) 200 Torr. The microplasma at 100 Torr shows the highest electron density inside the microcavity.

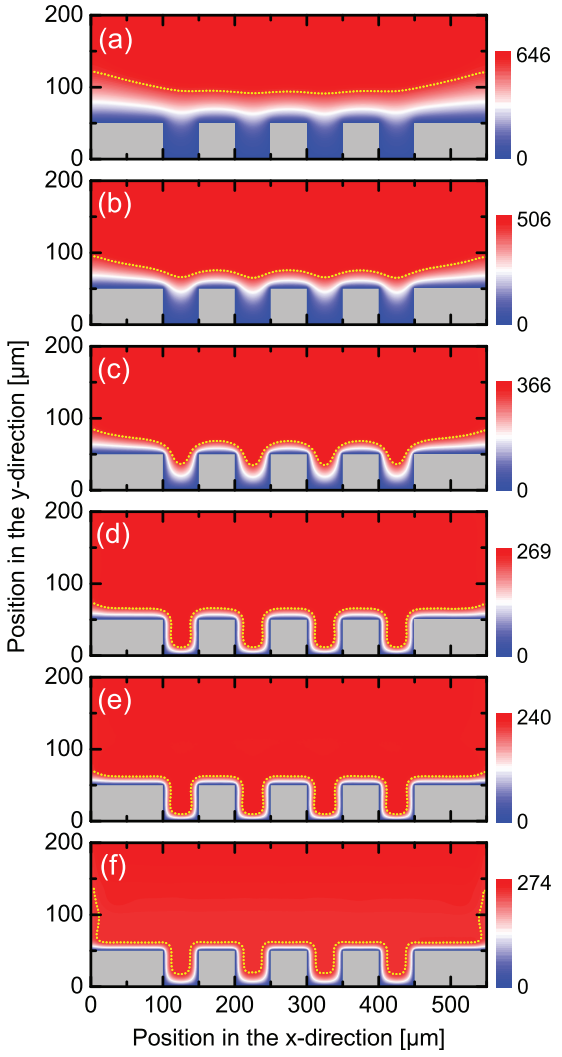

FIG. 3. Spatial distributions of the electric potential ϕ (unit in V) at (a) 10 Torr, (b) 20 Torr, (c) 50 Torr, (d) 100 Torr, (e) 150 Torr, and (f) 200 Torr. The contour line corresponds to $0.9\phi_{max}$ (ϕ_{max} is the maximum electric potential) in each case.

MHCDs [see Fig. 2(f)]. At 200 Torr, the dominant discharge region shifts outside the cathode microcavities, and the maximum electron density is reduced. The sheath width and the negative glow regions are obviously constricted due to the sufficiently high pressure. The opposite negative glow regions, which remain inside the microcavity, are separated without forming the typical MHCD. Note that here the sidewall is relatively far from the center, and thus, its effect on the plasma is less pronounced than the simulation using a single structure unit, in which the sheath width could be more comparable to the size of microplasma.

Figure 3 shows the spatial distributions of the electric potential, corresponding to the cases in Fig. 2. The contour (equipotential) line corresponds to $0.9\phi_{max}$ (ϕ_{max} is the maximum electric potential) in each case. In Figs. 3(a)–3(c), the dominant potential drop occurs outside of the microcavities; as the gas pressure increases, the equipotential line transits from flat to curved contour, which is also consistent with the gradually curved sheath edge [see Figs. 2(a)–2(c)]. In Figs. 3(d)–3(f), at higher pressures, the cathode fall layers are generally smaller, and most of the microgap domain, including the microcavity, is equipotential. The $0.9\phi_{max}$ potential drop width is very narrow for discharges in the MHCD mode [see Figs. 3(d) and 3(e)]. However, at 200 Torr, the voltage drop from the bottom becomes wider [see Fig. 3(f)] since the discharge does not penetrate sufficiently into the microcavities and the dominant discharge locates above the protrusion tips.

The transition behaviors of the microdischarges are observed in Figs. 2 and 3, which demonstrate the negative glow discharge with gradually curved sheath edge, hollow cathode discharge mode, and glow discharge with constricted cathode fall layer. The electron density is significantly increased when the MHCDs are formed. The

microdischarges at higher pressure are periodically coupled, forming array microplasmas localized inside the cathode microstructures. Although the simulation results may change under different discharge conditions, the transition characteristics, according to the similarity law,[36] are expected to be generally similar with the same characteristic length, e.g., Knudsen number λ/L, where λ is the mean free path and L is the physical dimension.[37] The discharge characteristics are largely determined by the electron mean free path, which is expressed as

$$\lambda_e(\varepsilon) = \frac{k_B T_g}{p\sigma_c(\varepsilon)}, \tag{1}$$

where k_B is the Boltzmann constant, T_g is the gas temperature, p is the gas pressure, and $\sigma_c(\varepsilon)$ is the collision cross section.[38] As indicated in Ref. 39, secondary electrons accelerated by the opposite sheaths should collide with neutral particles (at least one collision or ionization) in negative glow to sustain the hollow cathode discharge. Considering the negative glow size should be larger than λ_e, we have the upper limit of the electron mean free path $\lambda_{e,max} = w_2 - 2d_s$, where d_s is the sheath width that could also depend on the gas pressure and the discharge current density J, i.e., $d_s = d_s(p, J)$. The hollow cathode discharge cannot form if λ_e is too large (e.g., $\lambda_e > \lambda_{e,max}$), or $\lambda_{e,max} \leq 0$ [e.g., $w_2 \leq 2d_s$ in Figs. 2(a)–2(c)], where the negative glow cannot be housed inside the cavity. On the other hand, the MHCD cannot form if λ_e is too small [e.g., at 200 Torr in Fig. 2(f)]. Considering the opposite negative glow regions inside the cavity should not be completely separated, we have the lower limit of the electron mean free path $\lambda_{e,min} = w_2/2 - d_s$. As shown in Fig. 4(a), the mean free path for electron impact ionization λ_{iz} of secondary electrons is compared to the estimated range $(\lambda_{e,min}, \lambda_{e,max})$. The MHCD is observed when λ_{iz} is within or close to the estimated range; otherwise, the MHCD cannot form. Therefore, the discharge can only penetrate the microcavity, forming MHCD, at a certain pressure or pw_2 range. Although simplified, it is a straightforward prediction on the relation between the gas pressure and the discharge transition behavior, the validity of which is also confirmed.

According to Refs. 40 and 41, the estimated range of pw_2 for MHCD formation in argon should be 0.026–10 Torr · cm;[42] the prediction of which, however, does not take the negative glow region into consideration and may not be sufficiently accurate. The experimental results by Schoenbach *et al.* suggest pw_2 ranging from 0.53 to 5 Torr · cm.[8] Our simulation results suggest the range is about 0.25 to 1 Torr · cm, which is closer to the experimental results than the rough theoretical estimation. A more appropriate estimation, considering the negative glow width and $d_s = d_s(p, J)$, indicates that the upper limit for argon MHCD is 1.1 Torr · cm,[42] which is almost the same as ours. Note that though rather close, the PIC results and the experiments still have difference, which may be relevant to the different discharge configurations utilized. The coplanar cylindrical holes are used in Ref. 8, while the discharge at higher pressure can still form inside the microcavity, showing a ring structure but without the overlapping of the opposite negative glow regions,[43] which may overestimate the upper limit. Other geometrical parameters (e.g., w_1, d_1, and d_2) may also alter the pw_2 range for the MHCD formation. Our results based on the fully kinetic simulations clearly present the MHCD formation and conditions with the discharge transition behaviors captured, which are beneficial for optimizing microdischarge array devices across different pressure regimes.

The macroscopic discharge parameter scalings with gas pressure are shown in Fig. 4(b). As the pressure increases, the gap voltage V_{gap} decreases from 642 V to the lowest value 274 V, and then increases. The U-shaped scaling tendency is consistent with previous experimental results of MHCDs (e.g., Yamasaki *et al.*[44]); similar tendencies were also reported by Metel *et al.*[45] and Kolobov and Metel[46] for classical hollow cathode discharges, which also indicate the validity of the simulation results. Note that V_{gap} is close to but could be smaller than ϕ_{max}, as shown in Fig. 3, because of the plasma potential which is slightly positive to the anode.[47,48] The discharge current I_{dis} is within the range of 1.58∼5.63 mA, while the input power P_{in} ($P_{in} = V_{gap} \cdot I_{dis}$) varies nonmonotonically within the range of 1.01∼1.58 W. The discharges in the MHCD mode have higher electron densities, whereas the power consumption is not the highest, showing an optimized energy efficiency. The discharge power consumption is relatively small (on the level of several Watts), whereas the power density is high (up to hundreds kW cm^{-3}),[49] indicating the flexibility in scaling up the array configuration for developing portable plasma equipment.

Figure 5 shows the electron energy probability functions (EEPFs) in full space at different pressures, which are highly non-Maxwellian with boosted high energy tails. As the pressure increases, the boosted high energy tail generally becomes less pronounced, and the maximum electron energy decreases, which corresponds to the maximum sheath voltage drop. When electrons (e.g., secondary electrons) travel

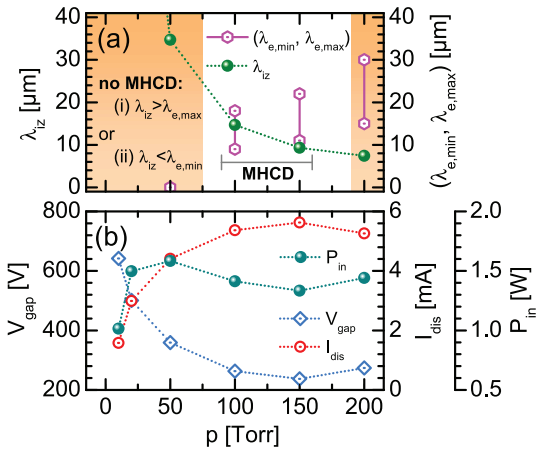

FIG. 4. (a) Comparison between the ionization mean free path and the estimated MHCD conditions. (b) Macroscopic discharge parameter scalings with gas pressure.

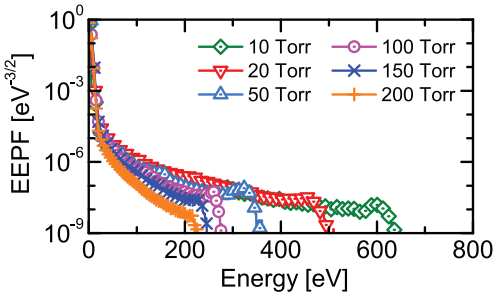

FIG. 5. EEPFs in full space at different pressures, which are highly non-Maxwellian with boosted high-energy tails.

across the sheath ballistically, they are accelerated and obtain the full potential energy, converting to kinetic energy.[50] At lower pressures, the electrons are more likely traveling ballistically, and maximum electron energy is close to the gap voltage. However, this is not necessarily true at higher pressures when the plasma becomes more collisional. For example, the gap voltage at 200 Torr is higher than that at 150 Torr, the maximum electron energy still decreases since the electrons may not travel across the sheath ballistically, thus not obtaining the full potential energy. Note that the high energy tail in the EEPFs is supposed to be little influenced by the numerical relaxation, due to the small physical relaxation time.[34]

In summary, we have demonstrated the formation and transition behaviors of microdischarges around microstructure arrays via two-dimensional PIC/MCC simulations. At the lowest pressure, the microplasma is outside the microcavities, and the sheath edge is relatively flat due to the space charge shielding effect. As the gas pressure increases, the sheath edge becomes curved and starts penetrating the microcavities on the cathode. At higher pressures, the MHCD is formed inside the microcavity and the electron density is significantly enhanced (order of 10^{21} m^{-3}). Further increasing the gas pressure results in the disappearance of the MHCD, and the dominant discharge region shifts to the outside of the microcavities. The condition of the MHCD formation is confirmed with the gradual discharge transition behaviors captured. In all the studied cases, the EEPFs in full space are highly non-Maxwellian and have boosted high energy tails, in which the highest energy corresponds to the maximum sheath potential drop. The microdischarges at higher pressures are localized to the cathode microstructures and coupled periodically, which indicates the flexibility in scaling up the microplasma array device toward larger dimension scales. The results from this study are helpful for more comprehensive understanding and better optimization of the operation of microplasma array devices in practical applications. The stability and tunability of the microdischarge interacting with a non-planar electrode surface morphology across a wider range of the discharge condition parameter regimes, and the effect of other electron emission mechanisms will be explored in future work.

AUTHORS' CONTRIBUTIONS

Y.F. and H.W. contributed equally to this work.

The authors are grateful to Professor Hae June Lee for fruitful discussions. This work was supported by the Air Force Office of Scientific Research Grant Nos. FA9550-18-1-0062 and FA9550-18-1-0061, the U.S. Department of Energy Office of Fusion Energy Science Grant No. DE-SC0001939, and the National Science Foundation Award Nos. 1917577 and 1724941. Xinxin Wang also acknowledges the support of the National Natural Science Foundation of China, Contract No. 51777114.

DATA AVAILABILITY

The data that support the findings of this study are available from the corresponding author upon reasonable request.

REFERENCES

[1]P. P. Sun, R. Zhang, W. Chen, P. V. Braun, and J. G. Eden, Appl. Phys. Rev. **6**, 041406 (2019).
[2]K. H. Schoenbach, A. El-Habachi, M. M. Moselhy, W. Shi, and R. H. Stark, Phys. Plasmas **7**, 2186 (2000).
[3]D. Janasek, J. Franzke, and A. Manz, Nature **442**, 374 (2006).
[4]H. Kabbara, S. Kasri, O. Brinza, G. Bauville, K. Gazeli, J. S. Sousa, V. Mille, A. Tallaire, G. Lombardi, and C. Lazzaroni, Appl. Phys. Lett. **116**, 171902 (2020).
[5]M. G. Kong, G. Kroesen, G. Morfill, T. Nosenko, T. Shimizu, J. Van Dijk, and J. L. Zimmermann, New J. Phys. **11**, 115012 (2009).
[6]J. Cheng, W. Ding, Y. Zi, Y. Lu, L. Ji, F. Liu, C. Wu, and Z. L. Wang, Nat. Commun. **9**, 3733 (2018).
[7]N. Y. Babaeva and M. J. Kushner, Plasma Sources Sci. Technol. **23**, 015007 (2014).
[8]K. H. Schoenbach, R. Verhappen, T. Tessnow, F. E. Peterkin, and W. W. Byszewski, Appl. Phys. Lett. **68**, 13 (1996).
[9]K. H. Schoenbach and K. Becker, Eur. Phys. J. D **70**, 29 (2016).
[10]K. H. Becker, K. H. Schoenbach, and J. G. Eden, J. Phys. D **39**, R55 (2006).
[11]A. Venkattraman, A. Garg, D. Peroulis, and A. A. Alexeenko, Appl. Phys. Lett. **100**, 083503 (2012).
[12]D. B. Go and A. Venkattraman, J. Phys. D **47**, 503001 (2014).
[13]J. Stephens, A. Fierro, B. Walls, J. Dickens, and A. Neuber, Appl. Phys. Lett. **104**, 074105 (2014).
[14]J. G. Eden and S.-J. Park, Plasma Phys. Controlled Fusion **47**, B83 (2005).
[15]S.-J. Park, K.-F. Chen, N. P. Ostrom, and J. G. Eden, Appl. Phys. Lett. **86**, 111501 (2005).
[16]J. G. Eden, S.-J. Park, J. H. Cho, M. H. Kim, T. J. Houlahan, B. Li, E. S. Kim, T. L. Kim, S. K. Lee, K. S. Kim, J. K. Yoon, S. H. Sung, P. Sun, C. M. Herring, and C. J. Wagner, IEEE Trans. Plasma Sci. **41**, 661 (2013).
[17]J. Hopwood, A. R. Hoskinson, and J. Gregório, Plasma Sources Sci. Technol. **23**, 064002 (2014).
[18]Z.-B. Zhang and J. Hopwood, Appl. Phys. Lett. **95**, 161502 (2009).
[19]C. Qu, P. Tian, A. Semnani, and M. J. Kushner, Plasma Sources Sci. Technol. **26**, 105006 (2017).
[20]T. Homola, V. Prukner, P. Hoffer, and M. Šimek, Plasma Sources Sci. Technol. **29**, 095014 (2020).
[21]V. A. Godyak and V. I. Demidov, J. Phys. D **44**, 233001 (2011).
[22]G. Kim, F. Iza, and J. K. Lee, J. Phys. D **39**, 4386 (2006).
[23]M. J. Kushner, J. Appl. Phys. **95**, 846 (2004).
[24]D. Levko and L. L. Raja, J. Appl. Phys. **119**, 163303 (2016).
[25]Y. Fu, B. Zheng, P. Zhang, Q. H. Fan, and J. P. Verboncoeur, J. Appl. Phys. **129**, 023302 (2021).
[26]F. Iza, J. K. Lee, and M. G. Kong, Phys. Rev. Lett. **99**, 075004 (2007).
[27]A. Semnani, A. Venkattraman, A. A. Alexeenko, and D. Peroulis, Appl. Phys. Lett. **103**, 063102 (2013).
[28]Y. Fu, P. Zhang, and J. P. Verboncoeur, Appl. Phys. Lett. **113**, 054102 (2018).
[29]Y. Fu, J. Krek, P. Zhang, and J. P. Verboncoeur, IEEE Trans. Plasma Sci. **47**, 2011 (2019).
[30]Y. Fu, P. Zhang, J. Krek, and J. P. Verboncoeur, Appl. Phys. Lett. **114**, 014102 (2019).
[31]B. Zheng, Y. Fu, D.-Q. Wen, K. Wang, T. Schuelke, and Q. H. Fan, J. Phys. D **53**, 435201 (2020).
[32]B. Zheng, K. Wang, T. Grotjohn, T. Schuelke, and Q. H. Fan, Plasma Sources Sci. Technol. **28**, 09LT03 (2019).
[33]M. M. Turner, Phys. Plasmas **13**, 033506 (2006).
[34]Z. Donkó, P. Hartmann, and K. Kutasi, Plasma Sources Sci. Technol. **15**, 178 (2006).
[35]G. Fubiani, G. J. M. Hagelaar, J. Boeuf, and S. Kolev, Phys. Plasmas **19**, 043506 (2012).
[36]Y. Fu and J. P. Verboncoeur, IEEE Trans. Plasma Sci. **47**, 1994 (2019).
[37]D. P. Lymberopoulos and D. J. Economou, J. Phys. D **28**, 727 (1995).
[38]M. A. Lieberman and A. J. Lichtenberg, *Principles of Plasma Discharges and Materials Processing* (John Wiley & Sons, New York, 2005).
[39]Y. Ohtsu and Y. Kawasaki, J. Appl. Phys. **113**, 033302 (2013).
[40]H. Helm, Z. Naturforsch. A **27**, 1812 (1972).
[41]J. W. Gewartowski and H. A. Watson, *Principles of Electron Tubes* (Van Nostrand, Princeton, NJ, 1965).
[42]K. H. Schoenbach, A. El-Habachi, W. Shi, and M. Ciocca, Plasma Sources Sci. Technol. **6**, 468 (1997).
[43]W. Shi, R. H. Stark, and K. H. Schoenbach, IEEE Trans. Plasma Sci. **27**, 16 (1999).

[44]T. Yamasaki, S. Namba, K. Takiyama, and H. Nojima, Jpn. J. Appl. Phys., Part 1 **51**, 066001 (2012).
[45]A. S. Metel, S. N. Grigoriev, Y. A. Melnik, and V. V. Panin, Plasma Phys. Rep. **35**, 1058 (2009).
[46]V. I. Kolobov and A. S. Metel, J. Phys. D **48**, 233001 (2015).
[47]Y. Fu, B. Zheng, D.-Q. Wen, P. Zhang, Q. H. Fan, and J. P. Verboncoeur, Appl. Phys. Lett. **117**, 204101 (2020).
[48]A. Bogaerts, E. Neyts, R. Gijbels, and J. Van der Mullen, Spectrochim. Acta B **57**, 609 (2002).
[49]A. Wollny, T. Hemke, M. Gebhardt, R. P. Brinkmann, H. Boettner, J. Winter, V. Schulz-von der Gathen, Z. Xiong, M. J. Kushner, and T. Mussenbrock, Appl. Phys. Lett. **99**, 141504 (2011).
[50]Y. Fu, B. Zheng, D.-Q. Wen, P. Zhang, Q. H. Fan, and J. P. Verboncoeur, Plasma Sources Sci. Technol. **29**, 09LT01 (2020).